INFERENCE OF HEATING PROPERTIES FROM "HOT" NON-FLARING PLASMAS IN ACTIVE REGION CORES II. NANOFLARE TRAINS

W. T. Barnes

Department of Physics & Astronomy, Rice University, Houston, TX 77251-1892

P. J. Cargill

Space and Atmospheric Physics, The Blackett Laboratory, Imperial College, London SW7 2BW and
School of Mathematics and Statistics, University of St. Andrews, St. Andrews, Scotland KY16 9SS

AND

S. J. Bradshaw

Department of Physics & Astronomy, Rice University, Houston, TX 77251-1892

Draft version June 25, 2016

ABSTRACT

Faint, high-temperature emission in active region cores has long been predicted as a signature of nanoflare heating. However, the detection of such emission has proved difficult due to a combination of the efficiency of thermal conduction, non-equilibrium ionization, and inadequate instrument sensitivity. In this second paper in our series on "hot" non-flaring plasma in active regions, we investigate the influence of repeating nanoflares of varying frequency on the resulting emission measure distribution . We have used an efficient two-fluid hydrodynamic model to carry out a parameter exploration in preferentially heated species, heating event frequency, and the power-law index determining the distribution of event energies. We compute the emission measure distribution for each point in our multi-dimensional heating parameter space in an effort to understand how each of these variables impacts the observed emission. Additionally, we calculate several observables and compare their efficacy in capturing the character of both the hot and cool parts of the emission measure distribution.

1. INTRODUCTION

Heating of the solar corona by nanoflares, first proposed by Parker (1988), has become one of the most favored and contentious coronal heating models (Cargill 1994; Cargill & Klimchuk 2004; Klimchuk 2006). The term *nanoflare* has now become synonomous with impulsive heating in the energy range $10^{24} - 10^{27}$ erg, with no specific assumption regarding the underlying physical mechanism; though its origin is almost certainly magnetic.

Cargill (1994); Cargill & Klimchuk (2004) have predicted that emission measure distributions resulting from nanoflare models should be wide and have a faint, high-temperature (8-10 MK) component, the so-called "smoking gun" of nanoflare heating. Though many workers (Reale et al. 2009; Schmelz et al. 2009; Miceli et al. 2012; Testa & Reale 2012; Del Zanna & Mason 2014; Petralia et al. 2014; Schmelz et al. 2015) have claimed evidence of this hot, faint component of the emission measure, poor spectral resolution (Testa et al. 2011; Winebarger et al. 2012) and non-equilibrium ionization (Bradshaw & Cargill 2006; Reale & Orlando 2008) have made a positive detection of nanoflare heating difficult. However, Brosius et al. (2014), using observations from the *EUNIS-13* sounding rocket, identified relatively faint emission from Fe XIX in a non-flaring active region (AR), suggesting temperatures of ~ 8.9 MK.

One strategy for constraining potential heating models is analysis of modeled and observed emission measure distributions in active region (AR) cores. Originally proposed by Jordan (1975), it is well-known that the emission measure, $\mathrm{EM}(T) = \int n^2 \mathrm{d}h$, scales as $\mathrm{EM}(T) \sim T^a$ over a temperature range $10^6 \lesssim T \lesssim T_m$, where T_m is the temperature at which $\mathrm{EM}(T)$ peaks. Observations have shown that $2 \lesssim a \lesssim 5$, with $T_m \approx 10^{6.5-6.6}$ (Warren et al. 2011, 2012; Winebarger et al. 2011; Tripathi et al. 2011; Schmelz & Pathak 2012; Del Zanna et al. 2015).

A similar scaling has been claimed for hot emission such that $\mathrm{EM} \propto T^{-b}$. Typically, this power-law fit to the emission measure is done "hotward" of the peak, usually in the range $T_m \lesssim T \lesssim 10^{7.2}$. However, measured values of these hotward slopes are poorly constrained due to both the magnitude of emission and the lack of available spectroscopic data in this temperature range (Winebarger et al. 2012). Warren et al. (2012), find $7 \lesssim b \lesssim 10$, with uncertainties of $\pm 2.5 - 3$, for 15 AR cores though Del Zanna & Mason (2014), using observations from the Solar Maximum Mission, claim larger values for b.

An important parameter for any proposed coronal heating mechanism is the frequency of energy release. Nanoflare heating is often classified as either *high-frequency* or *low-frequency* heating. In the case of high-frequency heating, $\langle t_N \rangle$, the time between successive events, is such that $\langle t_N \rangle \ll \tau_{cool}$, where τ_{cool} is the loop cooling time, and in the case of low-frequency heating $\langle t_N \rangle \gg \tau_{cool}$ (Cargill et al. 2015). Steady heating is just high-frequency heating in the limit $\langle t_N \rangle \to 0$.

The frequency of energy release in the solar corona is an important piece of evidence for determining the yet unknown coronal heating mechanism(s). However, measurement of the heating frequency, through both direct

and indirect means, has proved challenging. With regard to the direct evidence of reconnection-driven (DC) heating, only recently have observations provided sufficient resolution to resolve magnetic field braiding (Cirtain et al. 2013), a supposed precursor to bursty energy release. Additionally, while the resulting AR core emission measure distribution holds many clues as to how the coronal plasma is heated and cools, reconstructing these EM from spectroscopic and narrow-band observations is non-trivial, with different inversion methods often giving significantly different results (Landi et al. 2012; Aschwanden et al. 2015). Efforts to measure the heating frequency through intensity fluctuations in AR cores have proved similarly difficult (Ugarte-Urra & Warren 2014).

Hydrodynamic loop models, combined with sophisticated forward modeling, provide an accurate method for assessing a wide variety of heating scenarios and calculating observables. Such models of nanoflare-heated loops have found emission measure slopes consistent with those derived from observations. While Bradshaw et al. (2012) found that the full range of a could not be accounted for with low-frequency nanoflares, Reep et al. (2013) showed that using a tapered nanoflare train allowed for $0.9 \lesssim a \lesssim 4.5$. Cargill (2014), using a 0D loop model, investigated a large range of heating frequencies, $250 < \langle t_N \rangle < 5000$ s, and found that only when t_N was between a few hundred and 2000 seconds and proportional to the nanoflare energy could the full range of observed emission measure slopes be found.

In our first paper, Barnes et al. (2016) (Paper I, hereafter), we studied the effect of pulse duration, flux limiting, and NEI on hot emission from single nanoflares. We found that emission signatures of the heating are likely to be found in the temperature range $4 \lesssim T \lesssim 10$ MK. We now turn our attention to repeated impulsive events on a single strand.

In this second paper in our series on hot emission in AR cores, we use an efficient two-fluid hydrodynamic model to explore the effect of repeated impulsive heating events of varying frequency on the resulting EM(T). In particular, we look at how the hot emission is affected by heating preferentially the electrons or the ions, with events drawn from a power-law distribution versus uniform heating rates. Additionally, we investigate the effect of scaling the inter-event waiting time to the event energy and as well as how NEI may affect the presence of hot emission. We use an emission measure ratio, similar to that of Brosius et al. (2014), to assess the relative importance of hot emission over the entire range of power-law indices and heating frequencies. Section 2 discusses the numerical model we have used to conduct this study and the parameter space we have investigated. Section 3 shows the resulting emission measure distributions and diagnostics for the entire parameter space. In Section 4, we discuss the impacts of two-fluid effects, prenanoflare density, and NEI on these calculated observables and how they may be interpreted in the context of nanoflare heating. Finally, Section 5 provides some concluding comments on our findings.

2. METHODOLOGY

2.1. *Numerical Model*

1D hydrodynamic models are excellent tools for computing field-aligned quantities in coronal loops. However, because of the small cell sizes needed to resolve the transition region and consequently small timesteps demanded by thermal conduction, the use of such models in large parameter space explorations is made impractical by long computational runtimes (Bradshaw & Cargill 2013). We use the popular 0D enthalpy-based thermal evolution of loops (EBTEL) model (Klimchuk et al. 2008; Cargill et al. 2012a,b, 2015) in order to efficiently simulate the evolution of a coronal loop over a large parameter space. This model, which has been successfully benchmarked against the 1D hydrodynamic HYDRAD code of Bradshaw & Cargill (2013), computes, with very low computational overhead, time-dependent, spatially-averaged loop quantities.

In order to treat the evolution of the electron and ion populations separately, we use a modified version of the usual EBTEL equations. This amounts to computing spatial averages of the two-fluid hydrodynamic equations over both the transition region and corona. A full description and derivation of these equations can be found in the appendix of Paper I. The relevant two-fluid pressure and density equations are,

$$\frac{d}{dt}\bar{p}_e = \frac{\gamma - 1}{L}\left[\psi_{TR} - (\mathcal{R}_{TR} + \mathcal{R}_C)\right] + \quad (1)$$

$$k_B \bar{n} \nu_{ei}(\bar{T}_i - \bar{T}_e) + (\gamma - 1)\bar{Q}_e, \quad (2)$$

$$\frac{d}{dt}\bar{p}_i = -\frac{\gamma - 1}{L}\psi_{TR} + k_B \bar{n} \nu_{ei}(\bar{T}_e - \bar{T}_i) + \quad (3)$$

$$(\gamma - 1)\bar{Q}_i, \quad (4)$$

$$\frac{d}{dt}\bar{n} = \frac{c_2(\gamma - 1)}{c_3 \gamma L k_B \bar{T}_e}\left(\psi_{TR} - F_{ce,0} - \mathcal{R}_{TR}\right), \quad (5)$$

where $c_2 = \bar{T}_e/T_{e,a} \approx 0.9$, $c_3 = T_{e,0}/T_{e,a} \approx 0.6$, ν_{ei} is the electron-ion binary Coulomb collision frequency and ψ_{TR} is a term included to maintain charge and current and neutrality. These equations are closed by the equations of state $p_e = k_B n T_e$ and $p_i = k_B n T_i$. In the cases where we treat the plasma as a single-fluid, we use the original EBTEL model as described in Klimchuk et al. (2008); Cargill et al. (2012a).

The loop is heated by a prescribed heating function, applied to either the electrons ($\bar{Q}_e$) or the ions ($\bar{Q}_i$). Both species cool through a combination of thermal conduction ($F_{ce,0}$, $F_{ci,0}$) and an enthalpy flux to the lower atmosphere, with the electrons also undergoing radiative cooling ($\mathcal{R}_C$). In the case of conductive cooling, a flux limiter, $F = (1/2)fnk_B T V_e$, is imposed to mitigate runaway cooling in a low-density, high-temperature plasma. In all cases we use a saturation limit of $f = 1$. See Paper I for a discussion of how f is likely to effect the presence of hot emission in a nanoflare-heated plasma.

2.2. *Energy Budget*

We define our heating function in terms of a series of discrete heating events plus a static background heating to ensure that the loop does not drop to unphysically low temperatures and densities between events. Thus, for loop half-length L and cross-sectional area A, for a triangular heating pulse of duration τ, the total event energy is $\varepsilon = LAH\tau/2$, where H is the heating rate. Each run will consist of N heating events, each with peak
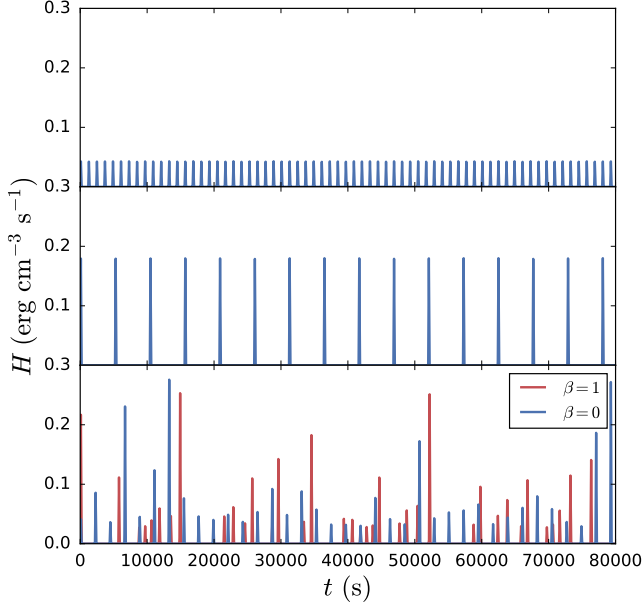
Fig. 1.— **Top**: uniform heating amplitudes for $t_N = 1000$ s; **Middle:** uniform heating amplitudes for $t_N = 5000$ s; **Bottom:** Heating amplitudes drawn from a power-law distribution with index $\alpha = -1.5$. The events shown in red have wait times that depend on the previous event energy while the events shown in blue have uniform wait times. The mean wait time in both cases is $\langle t_N \rangle = 2000$ s.

amplitude H_i, and a steady background value of $H_{bg} = 3.5 \times 10^{-5}$ erg cm^{-3} s^{-1}.

Recent observations have suggested that loops in AR cores are maintained at an equilibrium temperature of $T_{peak} \approx 4$ MK (Warren et al. 2011, 2012). Using our modified two-fluid EBTEL model, we have estimated the corresponding time-averaged volumetric heating rate for a loop of half-length $L = 40$ Mm to be $H_{eq} \sim 3.6 \times 10^{-3}$. In the single-fluid EBTEL model, this value is slightly lower because losses due to electron-ion collisions are ignored. Thus, to maintain an emission measure peaked about T_{peak}, for triangular pulses, the individual event heating rates are constrained by

$$H_{eq} = \frac{1}{t_{total}} \sum_{i=1}^{N} \int_{t_i}^{t_i+\tau} \mathrm{d}t\, Q(t) = \frac{\tau}{2t_{total}} \sum_{i=1}^{N} H_i, \quad (6)$$

where t_{total} is the total simulation time. Note that if $H_i = H_0$ for all i, the heating rate for each event is $H_i = H_0 = 2t_{total}H_{eq}/N\tau$. Thus, for $L = 40$ Mm, $A = 10^{14}$ cm^2, the average energy per event for a loop heated by $N = 20$ nanoflares in $t_{total} = 8 \times 10^4$ s is $\varepsilon = LAt_{total}H_{eq}/N \approx 5.8 \times 10^{24}$ erg, consistent with the energy budget of the Parker nanoflare model.

We define the heating frequency in terms of the waiting time, t_N, between successive heating events. Following Cargill (2014), the range of waiting times is $250 \leq t_N \leq 5000$ s in increments of 250 s, for a total of 20 different possible heating frequencies. Additionally, t_N can be written as $t_N = (t_{total} - N\tau)/N$, where we fix $t_{total} = 8 \times 10^4$ s and $\tau = 200$ s. Note that because t_{total} and τ are fixed, as t_N increases, N decreases. Correspondingly, $\varepsilon_i = LA\tau H_i/2$, the energy injected per event, increases according to Equation 6 such that the
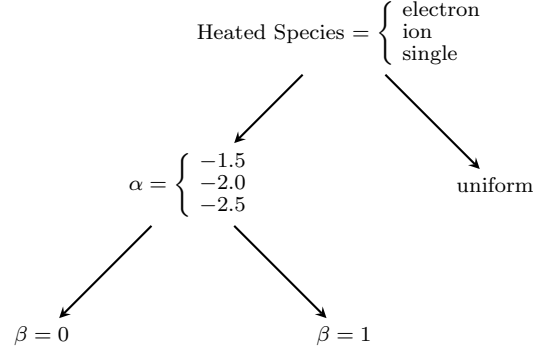

Fig. 2.— Total Parameter space covered. "single" indicates a single-fluid model. α is the power-law index and β indicates the scaling in the relationship $Q \propto T_N^\beta$, where $\beta = 0$ corresponds to the case where t_N and the event energy are independent. Note that (3 α values) $\times$ (2 β values) + uniform heating = 7 different types of heating functions.

total energy injected per run is constant, independent of t_N.

According to the nanoflare heating model of Parker (1988), turbulent loop footpoint motions twist and stress the field, leading to a buildup and subsequent release of energy. Following Cargill (2014), we let $\varepsilon_i \propto t_{N,i}^\beta$, where $\varepsilon_i, t_{N,i}$ are the total energy and waiting time following event i, respectively, and $\beta = 1$ such that the event energy scales linearly with the waiting time. The reasoning for such an expression is as follows. Bursty, nanoflare heating is thought to arise from the stressing and subsequent relaxation of the coronal field. If a sufficient amount of energy is released into the loop, the field will need enough time to "unravel" and "wind up" again before the next event such that the subsequent waiting time is large. Conversely, if only a small amount of energy is released, the field will require a shorter unwinding time, resulting in a shorter interval between the subsequent events. Thus, this scaling provides a way to incorporate a more physically motivated heating function into a hydrodynamic model which cannot self-consistently determine the heat input based on the evolving magnetic field. Figure 1 shows the various heating functions used for several example t_N values.

2.3. Heating Statistics

We compute the peak heating rate per event in two different ways: 1) the heating rate is uniform such that $H_i = H_0$ for all i and 2) H_i is chosen from a power-law distribution with index α where $\alpha = -1.5, -2.0$, or -2.5. For the second case, it should be noted that, when $t_N \approx 5000$ s, $N \sim 16$ events, meaning the events from a single run do not accurately represent the distribution of index α. Thus, a sufficiently large number of runs, N_R, are computed for each t_N to ensure that the total number of events is $N_{tot} = N \times N_R \sim 10^4$ such that the distribution is well-represented. Figure 2 shows the parameter space we will explore. For each set of parameters and waiting time t_N, we compute the resulting emission measure distribution for N events in a period t_{total}. This procedure is repeated N_R times until $N \times N_R \sim 10^4$ is satisfied. Thus, when $t_N = 5000$ s and $N \sim 15$, $N_R = 625$, meaning the model is run 625 times with a heating frequency of $t_N = 5000$ s in order

to properly fill out the event energy distribution.

2.4. *Non-equilibrium Ionization*

When considering the role of nanoflares in the production of hot plasma in AR cores, it is important to take non-equilibrium ionization (NEI) into account (Bradshaw & Cargill 2006; Reale & Orlando 2008). In a steady heating scenario, the ionization state is an adequate measure of the electron plasma temperature. Because the heating timescale is long (effectively infinite), the ionization state has plenty of time to come into equilibrium with the electron temperature.

In a nanoflare train, when the heating frequency is high, the loop is not allowed to drain or cool sufficiently between events, meaning the ionization state is kept at or near equilibrium. However, as the heating frequency decreases, the loop is allowed to cool and drain more and more during the inter-event period. If the heating occurs on a short enough timescale, the ionization state will not be able to reach equilibrium with the electron plasma before the loop undergoes rapid cooling by thermal conduction. Furthermore, if the frequency is sufficiently low so as to allow the loop to drain during the inter-event period, the ionization equilibrium timescale will increase. Thus, in the context of intermediate- to low-frequency nanoflares, NEI should be considered.

As in Paper I, we use the numerical code[1] outlined in Bradshaw (2009) to asses the impact of NEI on our results. Given a temperature $(T(t))$ and density $(n(t))$ profile from EBTEL, we compute the non-equilibrium ionization states for Fe IX through XXVII and the corresponding effective electron temperature, T_{eff} that would be inferred by assuming ionization equilibrium. Using T_{eff}, we are then able to compute a corresponding NEI emission measure distribution.

3. RESULTS

We now show the results of our loop simulations for each point in our multi-dimensional parameter space: species heated (single-fluid, electron or ion), power-law index (α), heating frequency (t_N), and waiting-time/event energy relationship (β). In each 0D hydrodynamic simulation, a loop of half-length $L = 40$ Mm is heated by N triangular events of duration $\tau = 200$ s and peak heating rate H_i for a duration of $t_{total} = 8 \times 10^4$ s. The average interval between subsequent events is t_N (in the uniform and power-law case, $t_N, i = t_N$ exactly for all i). We focus primarily on the emission measure distribution, $EM(T)$, and observables typically calculated from $EM(T)$. In all cases, the coronal emission measure is calculated according to the method outlined in section 3 of Paper I. The corresponding NEI results, $EM(T_{eff})$, are calculated similarly, but using T_{eff} (see Subsection 2.4) instead of T. All results were processed using the IPython system for interactive scientific computing in Python (Pérez & Granger 2007) as well as the NumPy and Scipy numerical and scientific Python libraries (van der Walt et al. 2011). All results were visualized using the matplotlib graphics library (Hunter 2007).

[1] This code has been made freely available by the author and can be downloaded at: https://github.com/rice-solar-physics/IonPopSolver.

3.1. *Emission Measure Distributions*

In our first set of results, we compare $EM(T)$ for three different types of heating functions, across six different heating frequencies. Figure 3, Figure 4, and Figure 5 show the emission measure distributions in the single-fluid case, electron heating case, and ion heating case, respectively. Each panel in each figure corresponds to a different waiting time (t_N) and includes three different types of heating functions: uniform heating events (red), events chosen from a power-law distribution of index $\alpha = -2.5$ (blue), and events chosen from a power-law distribution of index $\alpha = -2.5$ where the time between successive events depends on the heating rate of the preceding event (green). Furthermore, the dashed lines denote the corresponding NEI cases, $EM(T_{eff})$.

Recall from Subsection 2.3 that for those heating functions which choose peak heating rates from a power-law distribution, for each t_N, we run the model $N_R \sim (t_N+200)/8$ times. Thus, for each point in our parameter space, we produce N_R $EM(T)$ curves. In order to present our results compactly, the panels of Figure 3, Figure 4, and Figure 5 each show the average over all N_R curves. In this way, we account for the variations that may occur because of a lack/excess of strong heating events due to limited sampling from the distribution.

We look first at $EM(T)$ for the single-fluid case, Figure 3. Looking at all six panels, we note that as t_N increases, $EM(T)$ widens, extending to both cooler (< 4 MK) and hotter (> 4 MK) temperatures. $EM(T)$ extends toward cooler temperatures because as t_N increases and there is more time between successive heating events, the loop is allowed more time to cool both by radiation and enthalpy-driven cooling. $EM(T)$ extends towards hotter temperatures for similar, but more subtle reasons. As $t_N \to 0$, we approach the steady heating case in which conductive and radiative cooling exactly balance the heating. As t_N increases and becomes comparable to and greater than a cooling time, the loop beceomes increasingly tenuous at the time of the subsequent heating event, allowing the loop to reach much hotter temperatures since radiative cooling is very inefficient at low densities and the heat flux saturates. In this way, $EM(T)$ can "see" this greater range of temperatures, both hot and cool, provided it is allowed to undergo a typical heating and cooling cycle. The more curtailed this cycle is by continued reheatings, the more narrow $EM(T)$ will be.

Looking at the different curves in each panel of Figure 3, it is important to note that, although $EM(T)$ for all three types of heating functions widen with increasing wait time, their dependence on t_N is quite different. The uniform (red) and power-law (blue) $EM(T)$ curves evolve similarly as they extend to cooler temperatures with increasing t_N while the power-law, $\beta = 1$ curve (green) extends to cooler temperatures much more rapidly. For example, at $t_N = 1500$ s, both the uniform and power-law cases show little to no emission below 2 MK while the $\beta = 1$ cases extends to temperatures well below 1 MK (Cargill 2014). Contrastingly, on the hot side, the power-law and $\beta = 1$ curves evolve nearly identically with increasing t_N while the uniform heating case shows a cutoff at much lower temperatures, particularly for $t_N \leq 2500$ s.

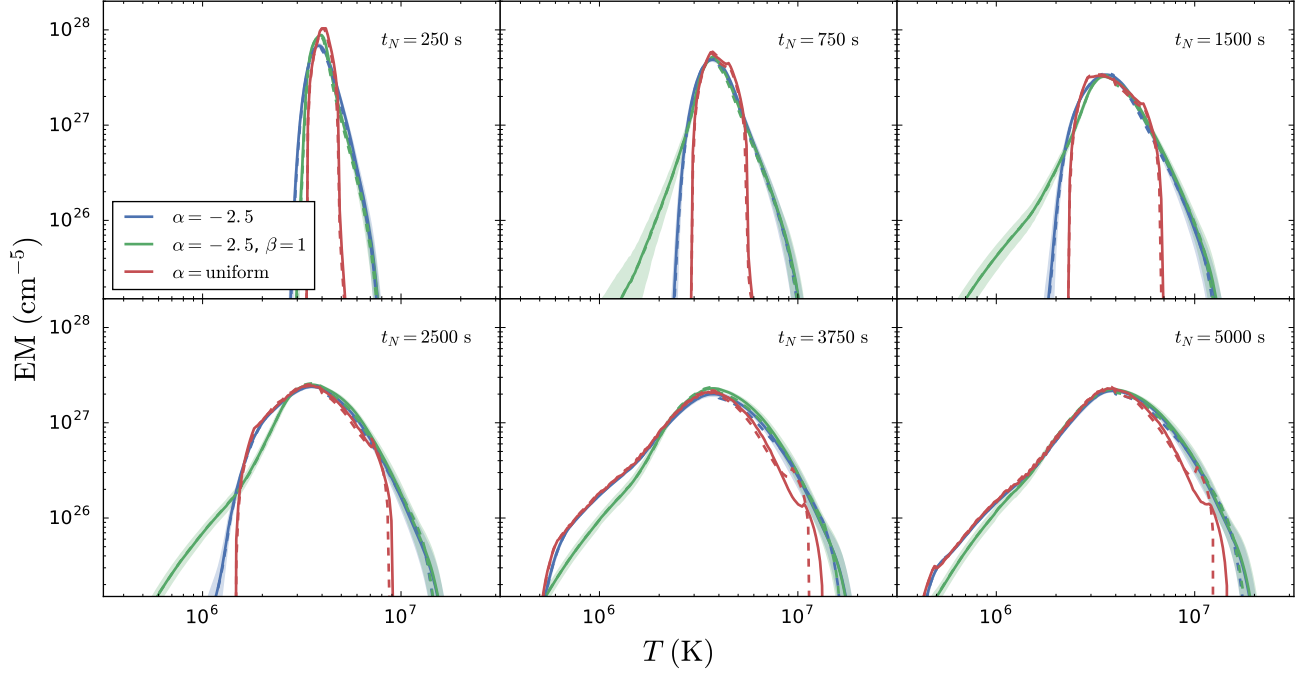The $EM(T)$ curves for the different types of heating

FIG. 3.— Emission measure distributions for waiting-times $t_N = 250, 750, 1500, 2500, 3750, 5000$ s in the single-fluid case. The three types of heating functions shown are uniform heating rates (red), heating rates chosen from a power-law distribution of $\alpha = -2.5$ (blue), and heating rates chosen from a power-law distribution of $\alpha = -2.5$ where the time between successive events is proportional to the heating rate of the preceding event (green). The solid lines in the power-law cases show the mean $\mathrm{EM}(T)$ over N_R runs and the shading indicates 1σ from the mean. The dashed lines denote the corresponding $\mathrm{EM}(T_{eff})$ distribution.

functions shown in Figure 4, in which only the electrons are heated, evolve similarly to those shown in Figure 3. This is particularly true on the cool side where the density is sufficiently high, allowing the electrons and the ions to equilibrate such that there is no discernible difference compared to the single-fluid case. On the hot side, for $t_N \leq 750$ s, the electron and single-fluid cases are quite similar. However, for $t_N \geq 1500$ s, $\mathrm{EM}(T)$ steepens just above 4 MK and then flattens out near 10 MK. This change in shape is most obvious in the uniform heating case where a distinct "hot shoulder" forms just above 10 MK. In the power-law cases, this feature is less pronounced and the $\mathrm{EM}(T)$ extends to slightly higher temperatures.

In Figure 5 in which only the ions are heated, the cool side of the $\mathrm{EM}(T)$ is very similar to both the single-fluid and electron heating cases because the electron and ion populations are in equilibrium during this portion of the loop's evolution. On the hot side, for intermediate to low heating frequencies (i.e. $t_N \geq 1500$ s), the $\mathrm{EM}(T)$ in the uniform heating case is truncated below 10 MK and in the power-law cases extends to just above 10 MK for the lowest heating frequency ($t_N = 5000$ s). This cutoff at lower temperatures is due to the fact that electrons cannot "see" the ions until they have cooled well below their peak temperature. This is discussed in Paper I though in the single-pulse cases, the cutoff occured at lower temperatures. Additionally, in both the uniform and power-law cases, the peak of the $\mathrm{EM}(T)$ is wider for these low frequencies compared to those cases shown in Figure 3 and Figure 4.

The dashed lines in the panels of Figure 3, Figure 4, and Figure 5 show the corresponding $\mathrm{EM}(T_{eff})$ for each heating function type. Only the mean $\mathrm{EM}(T_{eff})$ over

N_R runs is shown for these results. In all three figures, for the intermediate to high frequencies (i.e. $t_N \leq 1500$ s), there is no discernible difference between $\mathrm{EM}(T)$ and $\mathrm{EM}(T_{eff})$. Furthermore, both of the power-law cases show little deviation from ionization equilibrium in the emission measure for even the lowest heating frequencies in the single-fluid, electron heating, and ion heating cases. For $t_N \geq 2500$ s in the uniform heating case, in both Figure 3 and Figure 4, $\mathrm{EM}(T_{eff})$ is truncated at slightly lower temperatures as compared to $\mathrm{EM}(T)$. This hot emission is relocated to cooler temperatures, resulting in a "bump" in the emission measure distribution near 10 MK. None of the panels of Figure 5 show any significant difference between $\mathrm{EM}(T)$ and $\mathrm{EM}(T_{eff})$. This is because the electrons are essentially heated on a timescale dictated by the Coulomb collision frequency which is slow enough to ensure ionization equilibrium during the entire heating phase.

3.2. Pre-nanoflare Density

==Mostly discussing differences between power-law and uniform on hot side and scaling/non-scaling on the cool side. Lead into this paragraph from the previous paragraph. Questions to answer: why do power-law cases extend to hotter temperatures for equivalent t_N? Why do power-law cases show little to no deviation from IEQ?==

In the single-fluid and electron heating cases, while $\mathrm{EM}(T)$ in the uniform and power-law heating cases generally agree for low-frequency heating ($t_N = 5000$ s), for intermediate frequencies ($t_N \approx 750 - 2500$ s), the power-law cases show an enhanced high-temperature component compared to the uniform case as seen in Figure 3 and Figure 4.
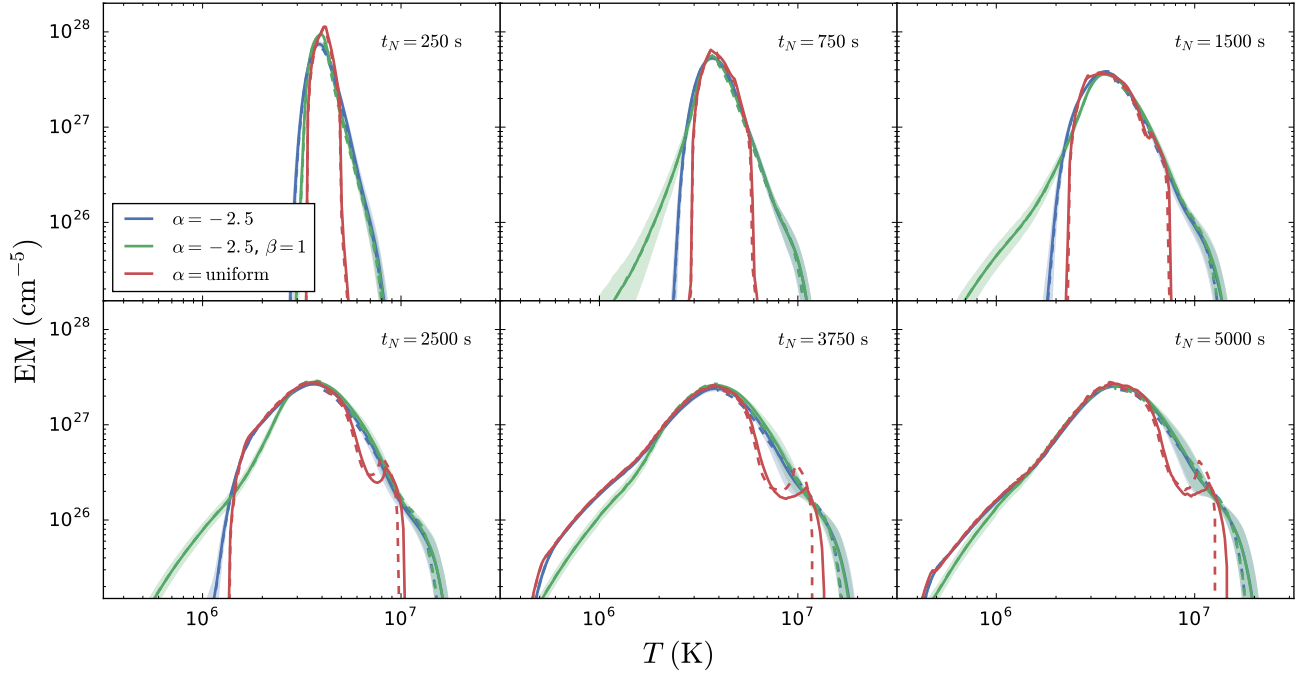
FIG. 4.— Same as Figure 3, but for the case where only the electrons are heated.
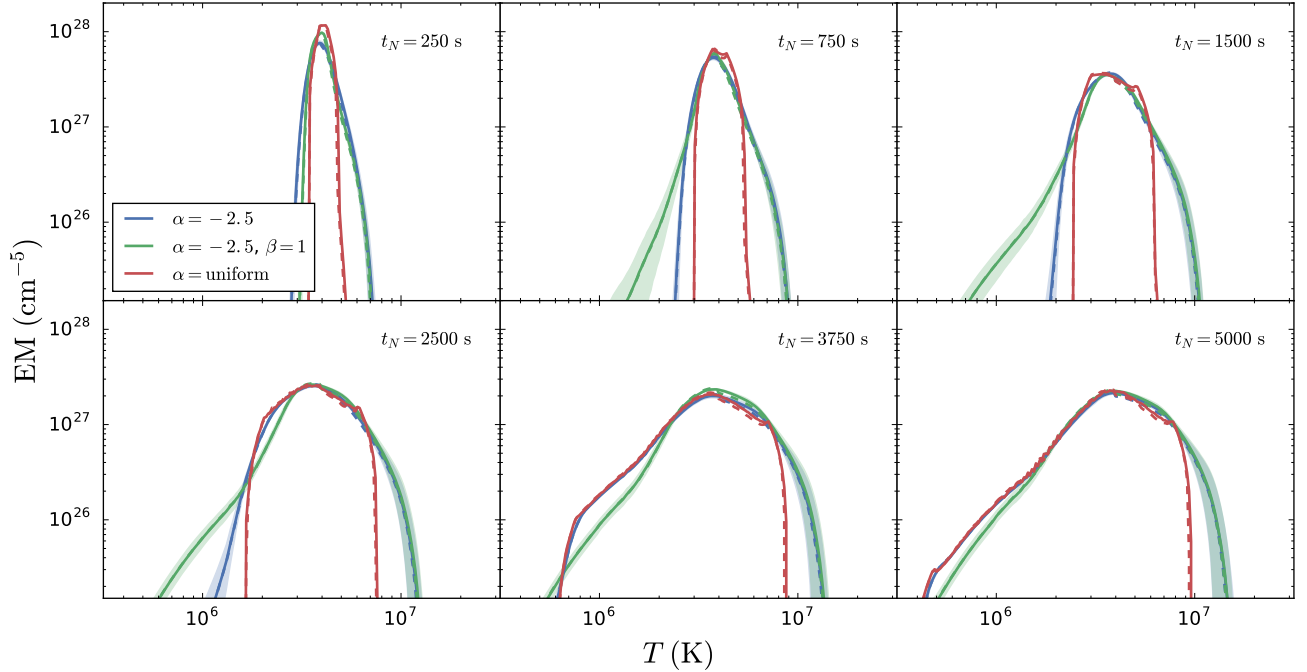

FIG. 5.— Same as Figure 3, but for the case where only the ions are heated.

Figure 6 shows sample heating, temperature, and density profiles for an intermediate heating frequency ($t_N = 2500$ s), in the case where only the electrons are heated, for the three different types of heating functions. In the uniform heating rate case (red), each event has a max heating rate of H_0 such that the loop undergoes $N \approx 30$ identical heating and cooling cycles, each time reaching a maximum temperature and density of $T_{max,0}$ and $n_{max,0}$, respectively. Recall from Equation 6 that the total energy injected into the loop is constrained such

that $H_0 = (1/N)\sum_{i=1}^{N} H_i$. In the case where the heating rates are distributed according to a power-law, there will be many events where $H_i < H_0$ and a few events where $H_i \gg H_0$.

The effect of these few higher energy events can be seen where the peak temperature of event i is greater than $T_{max,0}$ in the two power-law cases (blue and green curves) in the middle panel of Figure 6
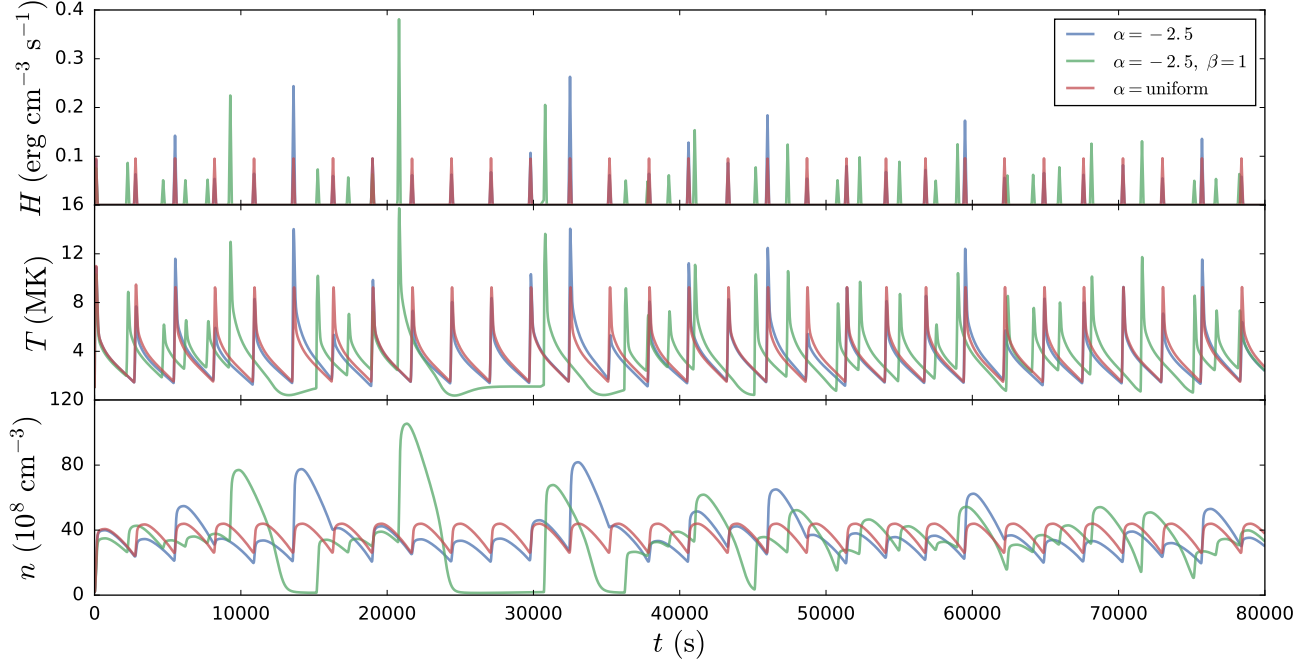
3.3. *Hot Plasma Diagnostics*

FIG. 6.— Example heating (top), temperature (middle), and density (bottom) profiles for the case in which only the electrons are heated and an intermediate heating frequency of $t_N = 2500$ s. The three curves shown in each panel correspond to uniform heating rates (red), heating rates chosen from a power-law distribution of $\alpha = -2.5$ (blue), and heating rates chosen from a power-law distribution of $\alpha = -2.5$ where the time between successive events is proportional to the heating rate of the preceding event (green).

Discuss usefullness of hot slope versus cool slope via figure; discuss advantages of em ratio; discuss em ratio figures; break into subsections?

We now examine several observables often used to characterize the emission measure distribution. The most common observable is the emission measure slope a such that EM $\propto T^a$ for $10^{5.5} \leq T \leq 10^{6.6}$ K. Both observational and modeling studies have found that $2 < a < 5$ (see Table 3 of Bradshaw et al. 2012) and in particular, Cargill (2014) found that a heating function of the form $t_N \propto \varepsilon$ was needed in order to account for this range of slopes. Additionally, a similar scaling of EM $\propto T^{-b}$ for $10^{6.6} \leq T \leq 10^{7.0}$ has been claimed though measurements of b have been subject to large uncertainties (Warren et al. 2012).

Figure 7 shows an example of how both T^a and T^{-b} can be fit to the cool and hot sides of EM(T), respectively. We fit log EM to $a \log T$ on $\log T_{c,min} < \log T < \log T_{c,max}$ and $-b \log T$ on $\log T_{h,min} < \log T < \log T_{h,max}$ using the Levenburg-Marquardt algorithm for least-squares curve fitting as implemented in the SciPy scientific Python package (van der Walt et al. 2011). We fix the lower limit on each interval such that $T_{c,min} = 10^{5.7}$ K and $T_{h,min} = 10^{6.7}$ K and vary the upper limits over $10^{6.1} < T_{c,max} < 10^{6.5}$ and $10^{6.8} < T_{h,max} < 10^{7.2}$. The left panel of Figure 7 shows the a (blue) and b (red) as a function upper limit of the fit interval, $T_{c,max}$ (bottom axis) and $T_{h,max}$ (top axis), respectively. The shading denotes the uncertainty of the fit. The right panel of Figure 7 shows the resulting fit lines superimposed on the emission measure distribution.

As seen in **??**, these histograms, denoted by type of slope (i.e. hot or cool) and species, are constructed in one of two ways: each distinct histogram (denoted by

linestyle and/or color) is either representative of a distinct heating function (e.g. top row of **??**) or a distinct value of t_N (e.g. bottom row of **??**). In the four panels of **??**, we choose to separate the cool emission measure slopes by type of heating function and the hot emission measure slopes by t_N. This means, for example, that the dot-dashed blue $\alpha = -1.5, \beta = 1$ histogram in the upper left panel of **??** encapsulates cool emission measure slopes for $250 \leq T_N \leq 5000$ s while the solid blue $T_N = 2000$ s histogram in the lower left panel includes emission measure slopes for all 10 types of heating functions (as listed in Figure 2 and the legend in the upper left panel of **??**). All histograms are normalized such that for each distribution $P(x)$, $\int_{-\infty}^{\infty} dx\ P(x) = 1$. Additionally, the bin widths are calculated using the well-known Freedman-Diaconis formula (Freedman & Diaconis 1981).

4. DISCUSSION

The main points we emphasize from the results presented in Section 3 are,

1. Cool emission measure slopes resulting from electron and ion heating are very similar and are well described by EM $\propto T^a$. As noted in Cargill (2014), using the relation $Q \propto T_N^\beta$ yields $2 \lesssim a \lesssim 5$, consistent with observations.

2. Hot emission from electron heating results in an enhanced hot shoulder while the equivalent ion heating cases show a relatively flat peak and a steep dropoff near 10^7 K. This effect is exacerbated as t_N increases.

3. Hot emission due to both electron and ion heating is poorly described by the scaling EM $\propto T^{-b}$. In the former, this is due to the flat hot shoulder between 10^7 and $10^{7.5}$ K. In the latter case, the
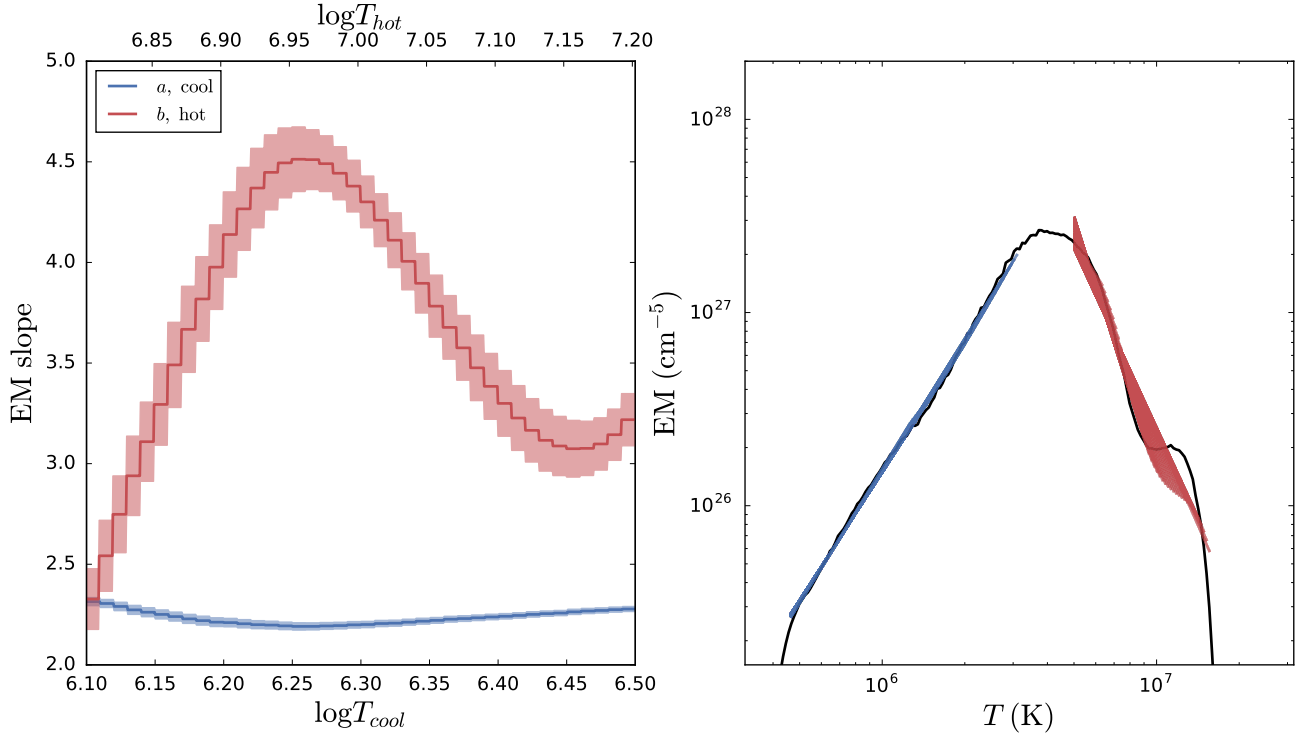
FIG. 7.— Power-law fits to a sample emission measure distribution constructed from a loop plasma in which only the electrons were heated by events chosen from a power-law distribution with $\alpha = -2.5$ and equally spaced by an interval of $t_N = 5000$ s. **Left:** EM(T) slope as a function of upper bound on fit interval for both the hot (red) and cool (blue) side of $EM(T)$. The shading denotes the uncertainty of the fit. The bottom axis corresponds to the varying upper limit on the fit to the cool side while the top axis corresponds to the varying upper limit on the fit to the hot side. **Right:** EM(T) with the overlaid hot (red) and cool (blue) fit lines whose slopes correspond to those shown on the left. The cool power-law fits describe describe EM(T) for $T < 4$ MK quite well while a similar fit on the hot side fails to accurately describe the shape of the emission measure distribution for $T > 4$ MK.
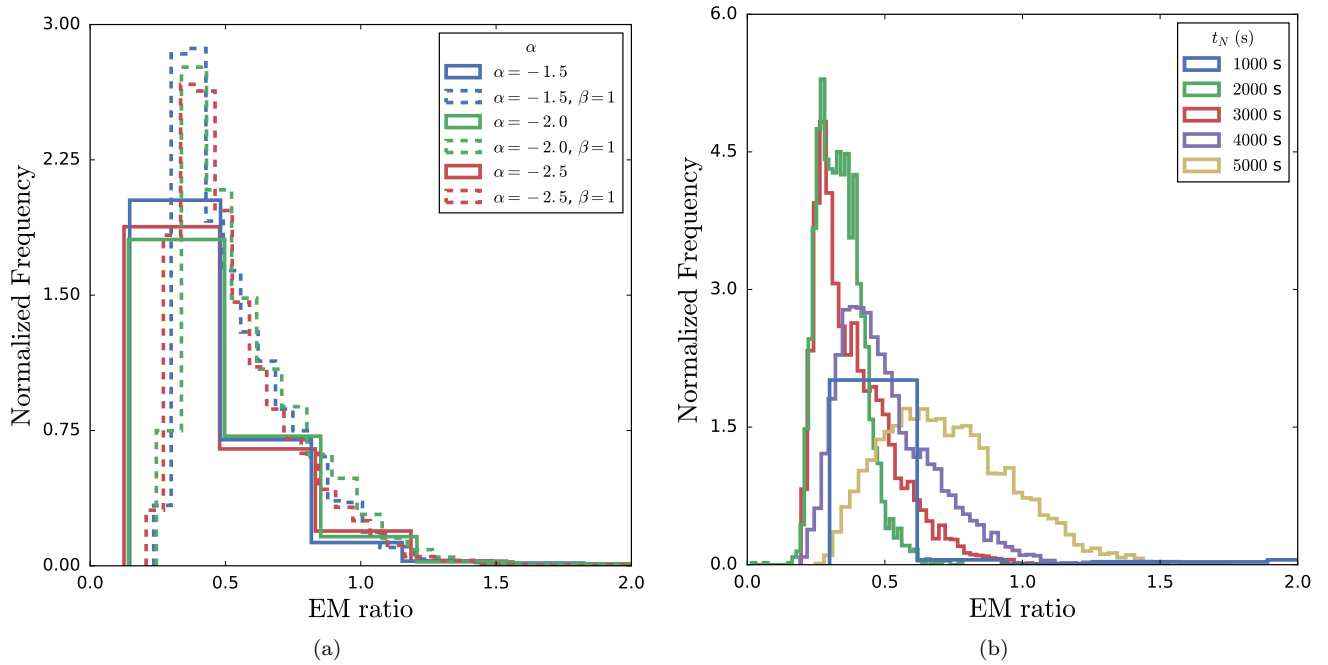

FIG. 8.— Electron heating emission measure ratio for an EIS/MaGIXS line pair. Need a more descriptive caption here!
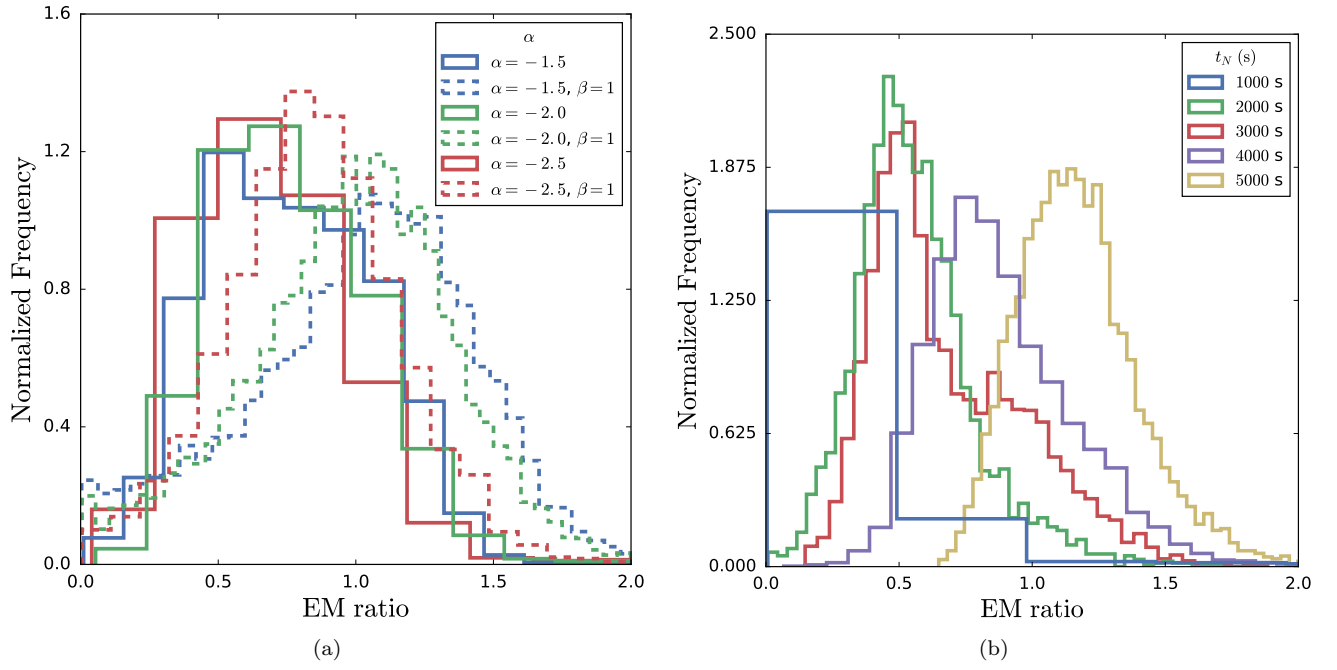
FIG. 9.— Diagnostics figures

relatively flat peak and steep drop off near 10^7 K do not allow for a power-law description of the hot emission.

4. Using a power-law to describe the hot side of the EM distribution, single-fluid models predict less hot-emission than two-fluid models in which only the electrons are heated. In particular, for $T_N \geq 4000$ s, our modified two-fluid EBTEL model predicts $3 \leq b \leq 3.5$ while the original single-fluid EBTEL model predicts $b \sim 4.5$.

5. Including NEI does not impact the cool emission measure slope. In the case of electron heating and the single-fluid case, NEI enhances the mid-range hot EM, but leads to a lower temperature cutoff. The emission measure distribution in the case of ion heating is unaffected.

We first focus on item 1. In the range $6.0 \leq \log T \leq 6.6$, the loop is undergoing both radiative and enthalpy-driven cooling. During this phase, the density is high and the temperature low relative to the heating and conductive cooling phase. Looking at the fourth term on the right-hand side of **??** and **??**, the coupling term between the two species is roughly $\propto \bar{n}^2(\bar{T}_e - \bar{T}_i)/\bar{T}_e^{3/2}$; as density increases, so does the coupling strength. While the loop is also draining in this temperature range, the density has already increased such that $\bar{T}_e \approx \bar{T}_i$ and until the next heating event, there is nothing to drive the two species out of equilibrium. Thus, because the two-species are evolving together in this regime, we expect their emission measure distributions to be the same.

In item 2, we see quite the opposite situation. In the heating and conductive cooling phases, the density is relatively low and the electron (or ion) temperature relatively high. Because the heating pulses we have used are relatively short (100 s), the heated species quickly reaches high temperatures and cools significantly by thermal conduction before Coulomb collisions can bring the two species back into equilibrium. Since the emission measure depends on the electron temperature, this means that in the event that only the electrons are heated, the emission "sees" the full range of temperatures produced by heating and conductive cooling.

However, in the case of ion heating, in order for the emission measure to see the full range of temperatures resulting from the heating and conductive cooling by the ions, $\bar{T}_e = \bar{T}_i$ would have to hold for this entire phase. Instead, as the ions are impulsively heated, the electrons remain at a relatively low temperature, coupled only weakly to the ions because the loop has only just begun to fill. As the coronal density increases, the electrons come into equilibrium with the ions, but because thermal conduction is such an efficient cooling mechanism in the corona, the ions have now cooled far below the temperature to which they were initially heated.

The result is a severely truncated hot emission measure distribution as seen in Figure 5. Additionally, this effect is exacerbated at long t_N. For short t_N, the heating is essentially steady, meaning that the loop has little to no time to drain or cool between heating events. This keeps the density at a roughly constant, near-equilibrium value which inhibits rapid heating to high temperatures and keeps the electrons and ions in equilibrium. However, for longer t_N, the loop is allowed to drain significantly

between each pulse. Thus, at the start of each heating event, the density is low, allowing the species to very quickly evolve out of equilibrium.

Finally, item 5 addresses the fact that NEI does not affect cool emission or emission due to ion heating, while it acts to enhance mid-range hot temperature emission and creates a lower-temperature cutoff in the single-fluid and electron heating cases as shown in **??**. As discussed in Paper I and Section 1, if the heating occurs on a timescale faster than the ionization equilibration timescale, high temperatures will not be detectable because the charge states indicative of such temperatures will not have had time to form. Coolward emission is due to radiative and enthalpy-driven cooling and during this phase, the density is relatively high and the temperature is changing relatively slowly, meaning that ionization equilibrium can be assumed.

For hotward emission in the case of ion heating, we note that the effective heating timescale for the electrons is approximately τ_{ei}, the coupling timescale. For $Q \approx 10^{25}$ erg, the electron temperature increases relatively slowly (compared to the heating timescale of the ions) and only gets above several MK once the density has increased significantly. Thus, ionization equilibrium can be assumed because the electrons undergo no direct impulsive heating. In the cases of electron heating and the single-fluid case, the electrons undergo direct impulsive heating when the density is relatively low. This is what leads to the lower-temperature cutoff in EM_{eff}: at these high temperatures and low densities, the ionization equilibrium timescale is significantly longer than the heating timescale and so these very high temperatures are never seen.

5. CONCLUSIONS

In this paper, we have used a modified two-fluid version of the popular EBTEL model to study the effect of preferentially heating the electrons or ions on the hot and cool emission measure slopes over a parameter space that includes the power-law index describing the distribution of event energies, α, waiting time between successive heating events, t_N, and the scaling between the event energy and wait time, β. We have found that while there is little difference in the cool emission between the cases of electron and ion heating, the emission measure curves of the electron-heated loops have an enhanced hot shoulder due to faster loop filling times and steepened hot mid-range slope due to accelerated cooling by the Coulomb collisions while the ion-heated loops show a truncated emission measure distribution on the hot side. These differences become more prominent as t_N increases. We note that given such a distinction in the EM distribution between the cases of electron and ion heating, the difference could be potentially observationally diagnosable by instruments such as MaGIXS, the Focusing Optics X-ray Solar Imager (FOXSI) (Krucker et al. 2011), or other future missions with adequate spectroscopic resolution in the hard X-rays.

Furthermore, by comparing these results with emission measure distributions obtained from the original single-fluid EBTEL model, we have found that heating only the electrons and using a single power-law fit leads to significantly smaller hot emission measure slopes for equivalent values of t_N. Thus, using a single-fluid model to interpret

observed hot emission measure distributions can potentially lead to a misdiagnosis of the heating frequency. Additionally, characterizing the hotward emission with a single power-law fit, as is common practice with cool emission, does not adequately capture all of the features of the hotward emission.

We note that in this study, we have constructed the most ideal emission measure curves by using the expression $EM = n^2(2L)$; that is, we have not taken into account the many complications involved when computing emission measure distributions from observed spectral lines. For example, as we noted in Paper I, impulsive heating leads to NEI and a consequently lower effective temperature, meaning that the emission does not see the hottest temperatures during the conductive cooling phase. By computing test cases for electron heating, ion heating, and the single-fluid case, we have shown that NEI has the effect of steepening the hot emission measure distribution at very high temperatures and enhancing the mid-range hot temperature emission for the electron heating and single-fluid cases, but has no impact on the emission measure distribution in the case of ion heating. We stress that when interpreting observed hot emission in the context of simulation, two-fluid and non-equilibrium ionization effects should be properly taken into account in order to extract meaningful properties of the heating.

ACKNOWLEDGMENT

REFERENCES

Aschwanden, M. J., Boerner, P., Caspi, A., et al. 2015, Solar Physics, 290, 2733
Barnes, W. T., Cargill, P. J., & Bradshaw, S. J. 2016, submitted
Bradshaw, S. J. 2009, Astronomy and Astrophysics, 502, 409
Bradshaw, S. J., & Cargill, P. J. 2006, Astronomy and Astrophysics, 458, 987
—. 2013, The Astrophysical Journal, 770, 12
Bradshaw, S. J., Klimchuk, J. A., & Reep, J. W. 2012, The Astrophysical Journal, 758, 53
Brosius, J. W., Daw, A. N., & Rabin, D. M. 2014, The Astrophysical Journal, 790, 112
Cargill, P. J. 1994, The Astrophysical Journal, 422, 381
—. 2014, The Astrophysical Journal, 784, 49
Cargill, P. J., Bradshaw, S. J., & Klimchuk, J. A. 2012a, The Astrophysical Journal, 752, 161
—. 2012b, The Astrophysical Journal, 758, 5
Cargill, P. J., & Klimchuk, J. A. 2004, The Astrophysical Journal, 605, 911
Cargill, P. J., Warren, H. P., & Bradshaw, S. J. 2015, Philosophical Transactions of the Royal Society of London Series A, 373, 20140260
Cirtain, J. W., Golub, L., Winebarger, A. R., et al. 2013, Nature, 493, 501
Del Zanna, G., & Mason, H. E. 2014, Astronomy and Astrophysics, 565, A14
Del Zanna, G., Tripathi, D., Mason, H., Subramanian, S., & O'Dwyer, B. 2015, Astronomy and Astrophysics, 573, A104
Freedman, D., & Diaconis, P. 1981, Zeitschrift für Wahrscheinlichkeitstheorie und Verwandte Gebiete, 57, 453
Hunter, J. D. 2007, Computing in Science & Engineering, 9, 90
Jordan, C. 1975, Solar Gamma-, X-, and EUV Radiation, 68
Klimchuk, J. A. 2006, Solar Physics, 234, 41
Klimchuk, J. A., Patsourakos, S., & Cargill, P. J. 2008, The Astrophysical Journal, 682, 1351
Krucker, S., Christe, S., Glesener, L., et al. 2011, in Society of Photo-Optical Instrumentation Engineers (SPIE) Conference Series, Vol. 8147, 814705

Landi, E., Reale, F., & Testa, P. 2012, Astronomy and Astrophysics, 538, A111
Miceli, M., Reale, F., Gburek, S., et al. 2012, Astronomy and Astrophysics, 544, A139
Parker, E. N. 1988, The Astrophysical Journal, 330, 474
Petralia, A., Reale, F., Testa, P., & Del Zanna, G. 2014, Astronomy and Astrophysics, 564, A3
Pérez, F., & Granger, B. E. 2007, Computing in Science & Engineering, 9, 21
Reale, F., & Orlando, S. 2008, The Astrophysical Journal, 684, 715
Reale, F., Testa, P., Klimchuk, J. A., & Parenti, S. 2009, The Astrophysical Journal, 698, 756
Reep, J. W., Bradshaw, S. J., & Klimchuk, J. A. 2013, The Astrophysical Journal, 764, 193
Schmelz, J. T., Asgari-Targhi, M., Christian, G. M., Dhaliwal, R. S., & Pathak, S. 2015, The Astrophysical Journal, 806, 232
Schmelz, J. T., & Pathak, S. 2012, The Astrophysical Journal, 756, 126
Schmelz, J. T., Saar, S. H., DeLuca, E. E., et al. 2009, The Astrophysical Journal Letters, 693, L131
Testa, P., & Reale, F. 2012, The Astrophysical Journal Letters, 750, L10
Testa, P., Reale, F., Landi, E., DeLuca, E. E., & Kashyap, V. 2011, The Astrophysical Journal, 728, 30
Tripathi, D., Klimchuk, J. A., & Mason, H. E. 2011, The Astrophysical Journal, 740, 111
Ugarte-Urra, I., & Warren, H. P. 2014, The Astrophysical Journal, 783, 12
van der Walt, S., Colbert, S. C., & Varoquaux, G. 2011, Computing in Science & Engineering, 13, 22
Warren, H. P., Brooks, D. H., & Winebarger, A. R. 2011, The Astrophysical Journal, 734, 90
Warren, H. P., Winebarger, A. R., & Brooks, D. H. 2012, The Astrophysical Journal, 759, 141
Winebarger, A. R., Schmelz, J. T., Warren, H. P., Saar, S. H., & Kashyap, V. L. 2011, The Astrophysical Journal, 740, 2
Winebarger, A. R., Warren, H. P., Schmelz, J. T., et al. 2012, The Astrophysical Journal Letters, 746, L17